J|A|C|S
JOURNAL OF THE AMERICAN CHEMICAL SOCIETY

pubs.acs.org/JACS Article

Electron Transfer Dynamics at Dye-Sensitized SnO_2/TiO_2 Core/Shell Electrodes in Aqueous/Nonaqueous Electrolyte Mixtures

Langqiu Xiao, Jacob A. Spies, Colton J. Sheehan, Zichen Zeng, Yunhan Gao, Tianyue Gao, Annika Ehrlacher, Michael W. Zuerch, Gary W. Brudvig, and Thomas E. Mallouk*

Cite This: J. Am. Chem. Soc. 2024, 146, 18117−18127 Read Online

ACCESS | Metrics & More | Article Recommendations | Supporting Information

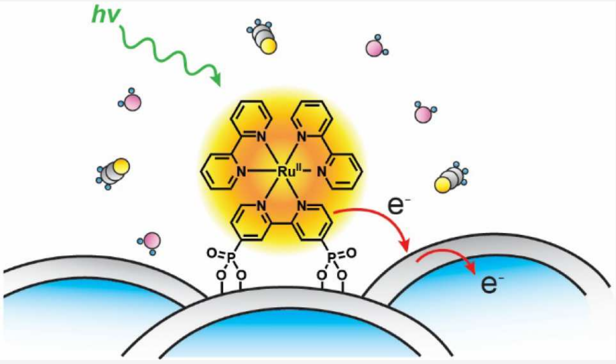

ABSTRACT: The dynamics of photoinduced electron transfer were measured at dye-sensitized photoanodes in aqueous (acetate buffer), nonaqueous (acetonitrile), and mixed solvent electrolytes by nanosecond transient absorption spectroscopy (TAS) and ultrafast optical-pump terahertz-probe spectroscopy (OPTP). Higher injection efficiencies were found in mixed solvent electrolytes for dye-sensitized SnO_2/TiO_2 core/shell electrodes, whereas the injection efficiency of dye-sensitized TiO_2 electrodes decreased with the increasing acetonitrile concentration. The trend in injection efficiency for the TiO_2 electrodes was consistent with the solvent-dependent trend in the semiconductor flat band potential. Photoinduced electron injection in core/shell electrodes has been understood as a two-step process involving ultrafast electron trapping in the TiO_2 shell followed by slower electron transfer to the SnO_2 core. The driving force for shell-to-core electron transfer increases as the flat band potential of TiO_2 shifts negatively with increasing concentrations of acetonitrile. In acetonitrile-rich electrolytes, electron injection is suppressed due to the very negative flat band potential of the TiO_2 shell. Interestingly, a net negative photoconductivity in the SnO_2 core is observed in mixed solvent electrolytes by OPTP. We hypothesize that an electric field is formed across the TiO_2 shell from the oxidized dye molecules after injection. Conduction band electrons in SnO_2 are trapped at the core/shell interface by the electric field, resulting in a negative photoconductivity transient. The overall electron injection efficiency of the dye-sensitized SnO_2/TiO_2 core/shell photoanodes is optimized in mixed solvents. The ultrafast transient conductivity data illustrate the crucial role of the electrolyte in regulating the driving forces for electron injection and charge separation at dye-sensitized semiconductor interfaces.

INTRODUCTION

Water-splitting dye-sensitized photoelectrochemical cells (WS-DSPECs) have been widely studied as a molecule-based system for light-driven generation of hydrogen from water.[1−3] This concept was built on the design of regenerative dye-sensitized solar cells (DSSCs), which were developed initially by Grätzel and coworkers in the mid-1980s.[4] While advances in silicon, compound semiconductor, and perovskite solar cells have eclipsed those of DSSCs over the past few years, the DSSC has recently struck back with a record-breaking power conversion efficiency of 15.2%.[5] Both WS-DSPECs and DSSCs involve ultrafast interfacial charge transfer steps, which are crucial for their energy conversion efficiency but are still not completely understood.

At the photoanodes of both WS-DSPECs and DSSCs, light-absorbing dye molecules (and water oxidation catalysts in the former case) are anchored to a high-surface area, mesoporous semiconductor, which is typically TiO_2. WS-DSPECs are operated in buffered aqueous solutions. Upon light excitation, the surface-adsorbed dye molecules inject electrons into the semiconductor conduction band, and the reduced form is regenerated by accepting electrons from water oxidation catalysts via intramolecular hole hopping.[6,7] In the initial examples of this concept, open circuit voltages close to 1.0 V were achieved, but the incident photon-to-current efficiency (IPCE) for water splitting was only 1−3%.[8−12] Mechanistic studies attributed the low efficiency to the slow kinetics of water oxidation catalysis relative to charge recombination at the dye-TiO_2 interface.[8,13−15] Core/shell electrode structures,[16] TiO_2 nanowire architectures,[17] fast molecular water oxidation catalysts,[18] and bilayer sensitizer/catalyst films[19] were subsequently developed, resulting in visible light IPCEs for water splitting in the range of 15%. Numerical modeling of

Received: April 15, 2024
Revised: May 29, 2024
Accepted: May 30, 2024
Published: June 20, 2024

the kinetics of a WS-DSPEC containing all of these optimized components suggested a limiting IPCE of ca. 17% in simulated sunlight.[20] In that case, the key limiting factors were the spectral overlap of the dye with sunlight and the initial electron injection efficiency. The latter was shown to be only about 30% in aqueous buffered solutions at pH 6.8,[6,21] which was the optimized pH for water oxidation catalysis. In contrast, DSSCs functionalized with the ruthenium bipyridyl dye N719, using an acetonitrile electrolyte solution with an iodide redox mediator and other additives, exhibit an electron injection efficiency of ca. 84%.[22] However, the injection efficiencies for DSSCs with dyes other than N719 are often lower at TiO_2 electrodes. Moreover, the core/shell electrode structures that have been investigated for DSSCs have improved chemical stability, but the electron injection efficiency can be significantly reduced due to the energetic barrier.[23] Thus, understanding the factors that control the electron injection efficiency could lead to substantial improvements in overall cell efficiencies, especially for WS-DSPECs.

Early studies of the DSSC employed aqueous electrolytes,[4] but they were supplanted by nonaqueous systems in the first high-efficiency cells.[24] Water was initially considered to be a detrimental contaminant in high-efficiency DSSCs. However, in an effort to replace the flammable and volatile nonaqueous electrolytes and achieve improved environmental compatibility, later studies on aqueous DSSCs made the community rethink the role that water plays.[25] O'Regan et al. discovered that the basic functions of DSSCs worked even in electrolytes with high water content. The presence of water in the electrolyte does not necessarily correlate with low efficiency and/or instability. The loss of photocurrent was mainly attributed to the lower current-carrying capability of the electrolyte in the pores of the semiconductor film, but water did not cause fundamental problems with electron transfer kinetics at the TiO_2/dye/electrolyte interface.[26]

In this work, we investigated the effects of mixed acetonitrile/aqueous electrolytes on the kinetics of electron injection at dye-sensitized mesoporous TiO_2 and SnO_2/TiO_2 core/shell electrodes by using nanosecond transient absorption spectroscopy (TAS) probed at 450 nm (where the maximum MLCT absorption peak of the dye is located) and ultrafast optical-pump terahertz-probe spectroscopy (OPTP). In addition to providing information on recombination dynamics, TAS actinometry[27] was used to quantify the injection efficiency from the perspective of the dye in contrast to the OPTP, which probes the relative injection efficiency from the perspective of the metal oxide.[28] The flat band potential of TiO_2, which depends on the solvent composition, modulates the driving force for electron injection and has a strong effect on its efficiency for TiO_2 electrodes. Hupp et al. have also shown that the intercalation of lithium ions into nanocrystalline TiO_2 shifts its conduction band edge to more positive potentials.[29] For core/shell electrodes, previous studies have shown that in aqueous media, the electron injection process occurs in two steps.[21,30] Ultrafast charge transfer from the photoexcited dye into TiO_2 trap states is followed by slower electron transfer to the SnO_2 core, and the latter process competes kinetically with back electron transfer to the oxidized dye molecule. By using ultrafast OPTP with picosecond time resolution to probe the injection process directly, we discovered a surprising effect in acetonitrile and mixed solvents. In these cases, a transient negative conductivity of the SnO_2 core is observed on the picosecond to nanosecond time scale. We attribute this transient to the trapping of intrinsic conduction band electrons in the SnO_2 core at the TiO_2-SnO_2 interface. We postulate that this depletion of charge carriers is driven by an electric field that is formed by charge injection, and thus, increased positive charge at the dye-TiO_2 interface. This effect is strongest in low-dielectric media, such as pure acetonitrile, but it also occurs in acetonitrile-aqueous electrolyte mixtures. By adjusting the electrolyte composition, we were able to optimize the effects of dielectric screening and flat band potential shift to maximize the electron injection efficiency of core/shell electrodes.

■ EXPERIMENTAL SECTION

Photosensitizer Synthesis. All reagents were used as received without further purification, unless otherwise noted. The synthesis of the photosensitizer was adapted from previous reports.[31,32] *cis*-Bis(2,2′-bipyridine)-dichlororuthenium(II) hydrate (0.12 g, 0.25 mmol, Sigma-Aldrich), 2,2′-bipyridine-4,4′-bis(diethylphosphonate) (0.16 g, 0.37 mmol, 98%, Carbosynth Ltd.), and 1:1 (v/v) ethanol/water (100 mL) were stirred and refluxed at 100 °C under an argon atmosphere for 6 h. The dark purple solution became dark orange-red and was allowed to cool to room temperature. The volume of the solution was then reduced to ca. 50 mL by rotary evaporation. The solution was then cooled in the refrigerator for 30 min. Ammonium hexafluorophosphate (80 mg, 0.49 mol, Sigma-Aldrich) was added to the solution to precipitate the product, and the solution was cooled at 0 °C overnight. The precipitate was vacuum filtered and dried in a vacuum oven overnight at 30 °C. A dark red powder was obtained.

Several batches of products (0.585 g, 0.51 mmol) were combined and mixed with anhydrous *N,N*-dimethylformamide (20 mL, 99.8%, Sigma-Aldrich) and bromotrimethylsilane (0.85 mL, 6.4 mmol, 97%, Sigma-Aldrich). The mixture was refluxed at 60 °C in the dark under an argon atmosphere for 18 h. The solvent and excess bromotrimethylsilane were removed under vacuum. Methanol (20 mL, 99.8%, Sigma-Aldrich) was added to the residue and stirred at room temperature for 3 h. To the deep orange solution, diethyl ether (99.8%, MilliporeSigma) was added until a dark red precipitate formed. The solvent was removed and the solid was washed with diethyl ether and dried in a vacuum oven. The pure product, bis(2,2′-bipyridine)(4,4′-diphosphonato-2,2′-bipyridine)-ruthenium(II) bromide, hereafter referred to as **RuP**, was obtained. ^1H NMR (500 MHz, CD_3OD, δ): 8.91 (d, 2H), 8.73 (d, 4H), 8.15 (t, 4H), 7.94 (t, 2H), 7.82 (t, 4H), 7.74 (m, 2H), 7.51 (4H).

The **RuP** photosensitizer was dissolved in 200 proof ethanol (Decon Laboratories, Inc.) and stored in the dark for future use.

Synthesis of TiO_2 and SnO_2 Nanoparticle Paste. The TiO_2 nanoparticle paste was made by following previous reported procedures.[33] The synthesis of the SnO_2 nanoparticle paste was adapted from the method reported by Grätzel et al.[34] In an agate mortar and pestle (diameter 9.5 cm), SnO_2 nanopowder (3 g, <100 nm average particle size, Sigma-Aldrich) was ground with water (0.5 mL) for 1 min. This step was repeated four more times. Ethanol (0.5 mL) was added to the mixture, which was ground for 1 min and this step was repeated 14 more times. Ethanol (1.25 mL) was added, and the mixture was ground for 1 min and repeated five more times. The SnO_2 paste was transferred to a beaker with 50 mL of ethanol and stirred with a stir bar for 1 min, followed by sonication with an ultrasonic horn (Branson Sonifier 450, 50% duty cycle, 5 output) for 2 min, then stirred with a stir bar for 1 min. Terpineol (10 g, anhydrous, Sigma-Aldrich) was added to the mixture, which was then stirred for 1 min, sonicated in the same manner as described above, and then stirred for an additional 1 min. Ethyl cellulose (1.5 g, 48−49.5% w/w, ethoxyl basis, Sigma-Aldrich) was added to ethanol (16.5 mL) and stirred vigorously until dissolved. Then the solution was added to the paste and stirred for 1 min, sonicated in the same manner described above, and then stirred for an additional 1 min. The stirring and sonication steps were repeated two more times, and excess ethanol was removed by rotary evaporation to yield the SnO_2 paste.

Preparation of TiO_2 and SnO_2/TiO_2 Core/Shell Electrodes. Fluorine-doped tin oxide (FTO) glass (TEC-8, Hartford Glass) was cleaned by sonicating in soapy water and then rinsed with DI water, followed by UV ozone cleaning. Scotch tape was applied as a spacer to control the thickness of the film. TiO_2 or SnO_2 paste was then applied to the clean FTO slides by the doctor-blading method.[35] TiO_2 nanoparticle electrodes were sintered by heating to 300 °C at 9 °C/min, held at 300 °C for 20 min, heated to 350 °C at 5 °C/min, held at 350 °C for 10 min, heated to 500 °C at 7 °C/min, and then held at 500 °C for 30 min.[33] The SnO_2 nanoparticle electrodes were sintered by heating to 370 °C at 3 °C/min, held at 370 °C for 10 min, heated to 470 °C at 3 °C/min, and then held at 470 °C for 30 min.[30]

The TiO_2 shell for the SnO_2 particles was fabricated by using a Cambridge NanoTech S200 atomic layer deposition (ALD) system. Tetrakis(dimethylamido)titanium was used as the precursor and was heated at 75 °C. The deposition was done at 150 °C. The pulse durations for water and the TiO_2 precursor were 0.1 and 0.015 s, respectively, with 20 s intervals between pulses. The cycles were repeated for 60 iterations. The deposition thickness was checked by measuring the TiO_2 layer deposited on a clean silicon wafer using ellipsometry. After the deposition, the electrodes were sintered at 450 °C for 30 min.

Characterization of SnO_2/TiO_2 Core/Shell Particles. The SnO_2/TiO_2 core/shell structure was characterized by scanning/transmission electron microscopy (S/TEM) and energy dispersive X-ray spectroscopy (EDS) on a JEOL JEM-F200. Images are shown in Figures S1 and S2.

Preparation of TiO_2 and SnO_2/TiO_2 Core/Shell Photosensitized Electrodes. The TiO_2 and SnO_2/TiO_2 core/shell electrodes were sensitized by immersing in a 0.1 mM **RuP** solution in ethanol, as described in a previous report.[17] The dye loading was measured by transmission UV−visible spectroscopy of the dye-sensitized electrodes (Agilent, Cary 6000i) (Figure S3). After sensitization, the electrodes were used directly for transient absorption measurement under an open-circuit condition. For the photoelectrical and flat band potential measurements, the electrodes were connected to insulated copper wires using silver paste (DuPont 4922N). The electrical contact and exposed FTO glass were sealed with white epoxy adhesive (Loctite EA 1C) and then Gorilla clear epoxy.

Nanosecond Transient Absorption Spectroscopy. Transient absorption spectroscopy measurements were carried out using an enVISion transient absorption system (Magnitude Instruments, State College, PA), which consisted of a pulsed frequency doubled (532 nm) Nd:YAG laser operating at a repetition rate of 400 Hz with a pulse energy of 210 μJ/pulse. A continuous-wave xenon lamp was used as the probe light source. The probe light source was dispersed through a monochromator and detected by a photodiode detector.

Photosensitized slides were placed diagonally at 45° in a standard 10 mm light path fluorescence cuvette, which was fused with a glass joint. Electrolyte mixtures were made by mixing 0.1 M sodium acetate buffer (pH 4.6) and 0.1 M tetra(*n*-butyl) ammonium perchlorate (≥99.0%, Sigma-Aldrich) in anhydrous acetonitrile (99.8%, Sigma-Aldrich) solution with volume ratios of 0/100, 25/75, 50/50, 75/25, and 100/0. The electrolytes were purged with argon for 5 min and then sealed with rubber septa before measurements.

For temperature-dependent measurements at open circuit, after purging the electrolyte mixtures with argon for 5 min, the cuvette was sealed and placed in a temperature-controlled cuvette holder (qX3/stnd, Quantum Northwest). For the analysis of the kinetic data of the temperature-dependent measurements, spectral data after 1000 ns were used for fitting to avoid interference from dye molecule absorbance in the excited state. The excited state lifetime of the molecules at different temperatures was also measured (Figure S4).

Optical-Pump Terahertz-Probe Spectroscopy. The samples for optical-pump terahertz-probe spectroscopy (OPTP) measurements were prepared using the same TiO_2 and SnO_2/TiO_2 particle pastes that were used for the transient absorption spectroscopy experiments. The nanoparticle pastes were doctor bladed onto a 0.1 cm thick, 2.54 cm × 2.54 cm quartz substrate (GM Quartz). For TiO_2 samples, the quartz substrates were pretreated with 60 cycles of ALD TiO_2 before applying the nanoparticle paste for better adhesion of the film to the substrate. The annealing and dye deposition were done as previously described for other samples. Samples in electrolytes were prepared by sealing the sample using a second quartz substrate with a 60 μm Surlyn spacer (Solaronix). The samples were then vacuum backfilled with electrolyte as previously described.[36]

OPTP measurements were performed with a home-built instrument based on a $Ti:Al_2O_3$ chirped-pulse regenerative amplifier (Spectra Physics Spitfire Ace, 800 nm center wavelength, 1 kHz repetition rate, 4 mJ pulse energy, 35 fs pulse duration) as previously described.[37,38] Briefly, the output of the laser system was split into three beams for generation of terahertz (THz) radiation in a two-color air plasma,[39,40] detection of THz radiation by free-space electro-optic sampling in a ZnTe (110) crystal,[41] and optical photoexcitation, respectively. Samples were photoexcited at 400 nm (frequency doubled in β-barium borate) with a pulse energy of 200 μJ corresponding to an effective fluence of 470 μJ cm^{-2} considering the pump and probe spot sizes (0.515 and 0.071 cm $1/e^2$ radius, respectively).

Measurements of Flat Band Potentials. The flat band potentials of the semiconductor electrodes were measured by a previously reported spectroscopic method.[42,43] The three-electrode system was set up in the same cuvette that was used in TAS measurement. The working electrodes were **RuP**-sensitized TiO_2 or SnO_2/TiO_2 core/shell electrodes. The working electrodes for the pure acetonitrile electrolyte were not sensitized to prevent reduction of **RuP**. The reference electrode was Ag/AgCl (3 M KCl) (Basi), and a platinum coil was used as the counter electrode. The reference electrode was calibrated by cyclic voltammetry of ferrocene in acetonitrile/tetra(*n*-butyl)ammonium perchlorate (Figure S5). For experiments in acetonitrile solutions, a fritted glass tube filled with 0.1 M tetra(*n*-butyl)ammonium perchlorate in acetonitrile was used as a salt bridge between the reference electrode and the electrolyte. The components of the electrolytes were aqueous sodium acetate buffer (0.1 M, pH 4.6) and 0.1 M tetra(*n*-butyl)ammonium perchlorate in acetonitrile solution. The working electrode was placed diagonally in the cuvette with the electrolyte. A cathodic linear scan at a rate of 1 mV/5 s was applied by a Metrohm Autolab potentiostat (PGSTAT128N), and the absorption at 780 nm was monitored by a UV−vis spectrometer (Agilent, Cary 6000i).

Measurement of the Reduction Potential of $RuP^{3+/2+}$ on Electrode Surfaces. ITO (In_2O_3:Sn) electrodes were prepared according to reported methods.[44] Briefly, ITO paste was doctor bladed onto clean FTO glass slides and dried in air for 30 min before heating at 450 °C in air for 1 h. The ITO on FTO slides were made into electrodes following the same procedures used for TiO_2 or core/shell electrodes. The working electrode, the Ag/AgCl (3 M KCl) reference electrode, and the platinum wire counter electrode were set up in the electrolyte solutions and purged with argon for 5 min. Cyclic voltammetry was performed under argon at a scan rate of 50 mV/s.

■ RESULTS

Relative photoinduced electron injection efficiencies of dye-sensitized electrodes were measured in acetonitrile and acetonitrile-aqueous buffer mixtures by thin film actinometry using nanosecond TAS, as previously reported:[45,46]

$$\phi_{\text{inj}} = \frac{\dfrac{\Delta A_{\text{sam}}(\lambda_p)}{\Delta\varepsilon_{\text{sam}}(\lambda_p)(1 - 10^{-\Delta A_{\text{sam}}(\lambda_{\text{ex}})})}}{\dfrac{\Delta A_{\text{ref}}(\lambda_p)}{\Delta\varepsilon_{\text{ref}}(\lambda_p)(1 - 10^{-\Delta A_{\text{ref}}(\lambda_{\text{ex}})})}} \times 100\% \tag{1}$$

Here, $\Delta A(\lambda_p)$ is the amplitude of the transient absorption signal at the probe wavelength (λ_p), $\Delta\varepsilon(\lambda_p)$ is the molar extinction coefficient difference between ground and oxidized states of the dye molecule, and $1 - 10^{-\Delta A(\lambda_{ex})}$ is the sample absorbance at the excitation wavelength (λ_{ex}).

Dye-sensitized electrodes in 0.1 M $HClO_4$ were used as the reference for 100% injection efficiency.[45,47] Assuming that the molar extinction coefficient and the sample absorbance are the same because the same dye molecule is used, eq 1 can be simplified as:

$$\phi_{\text{inj}} = \frac{\Delta A_{\text{sam}}(\lambda_p)}{\Delta A_{\text{ref}}(\lambda_p)} \times 100\% \tag{2}$$

The bleaching signals of the dye at the probe wavelength were fitted to a triexponential decay function, modeling the back electron transfer to the dye molecules occurring from various trap states:

$$\Delta A = A_1 \exp\left(-\frac{t}{\tau_1}\right) + A_2 \exp\left(-\frac{t}{\tau_2}\right) + A_3 \exp\left(-\frac{t}{\tau_3}\right) \tag{3}$$

The time traces of the transient absorption measurements probed at 450 nm and the fit parameters are shown in Figure 1 and Tables S1, S2, respectively. The amplitudes of the bleaching recovery for both electrode structures were normalized to the reference (dye-sensitized electrodes measured in 0.1 M $HClO_4$). The amplitude of the bleaching signal is proportional to the electron injection efficiency. For both structures, the injection efficiency in pure acetonitrile was the lowest. For mesoporous TiO_2 electrodes (Figure 1A), the injection efficiency increases with the concentration of the aqueous buffer, and for the core/shell structure (Figure 1B), the trend is the opposite. Notably, at ambient temperature, the back electron transfer kinetics in mixed electrolytes are all comparable, while the back electron transfer in pure acetonitrile is the fastest. The calculated photoinduced electron injection efficiencies are plotted in Figure 1C.

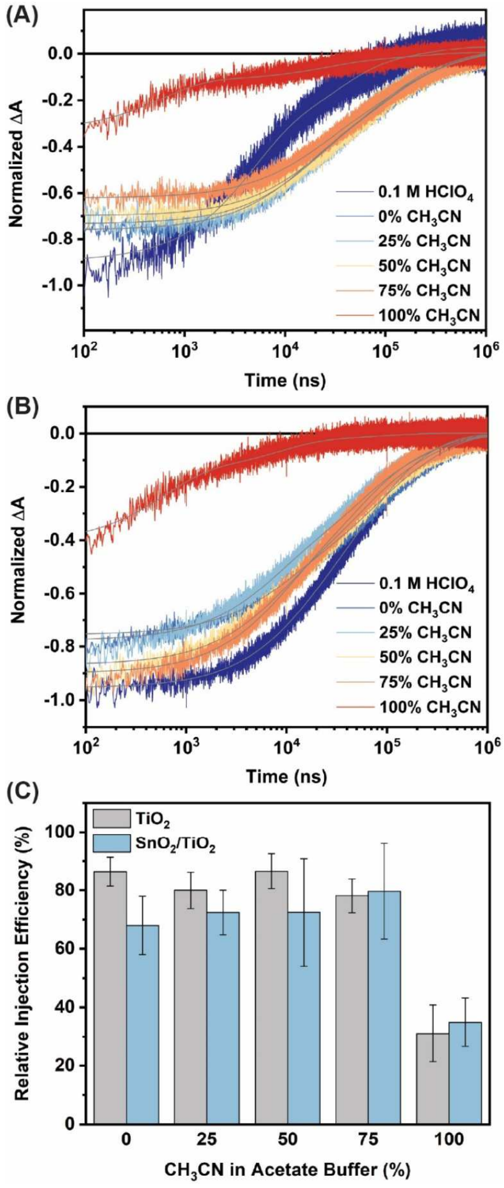

Figure 1. Normalized bleaching recovery monitored at 450 nm of (A) FTO|TiO_2|**RuP**, (B) FTO|SnO_2|TiO_2|**RuP**, and (C) relative electron injection efficiencies for both electrode structures measured in acetonitrile/aqueous sodium acetate buffer (0.1 M, pH 4.6) solutions with different fractions. Excitation: 532 nm, 210 μJ/pulse.

Back electron transfer rates were measured as a function of temperature under open-circuit conditions. The fastest term of the recombination kinetics as a function of temperature (the Arrhenius plot) is shown in Figures S9 and S10. For TiO_2 electrodes, charge recombination is fastest in a perchloric acid aqueous solution. This is consistent with the results of McCool et al., who observed fast recombination from the proton-induced trap states in TiO_2.[33] The temperature-independent charge recombination behavior in the core/shell structure indicates that charge transfer occurs predominately through a tunneling mechanism, consistent with an earlier study.[48]

While nanosecond TAS is limited to monitoring the back electron transfer process, OPTP is an ultrafast technique that probes the transient photoconductivity resulting from interfacial electron transfer into the metal oxide. THz radiation is attenuated by the presence of mobile carriers, which makes it sensitive to the electron injection kinetics and yield of mobile electrons in the material. Figure 2 shows the OPTP results for **RuP**-sensitized TiO_2 and SnO_2/TiO_2 core/shell structures as a function of mixed solvent electrolyte composition. A summary of the fit parameters discussed below is shown in Tables S3−S5.

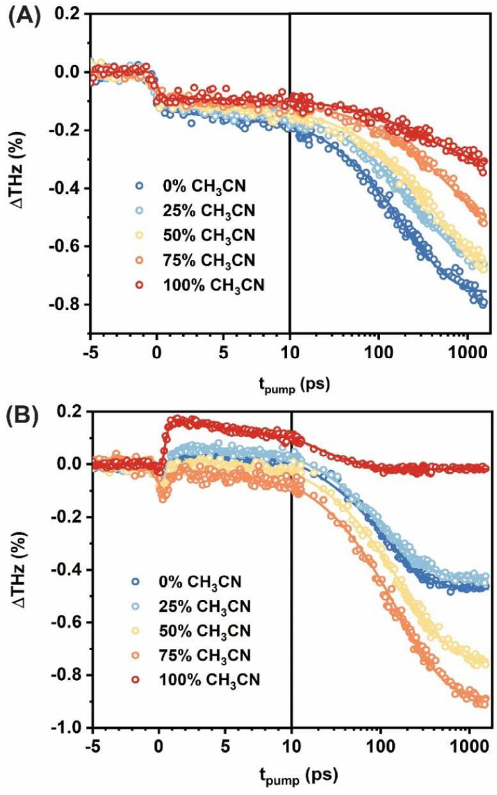

Figure 2. Optical-pump THz-probe (OPTP) measurements of **RuP**-sensitized (A) TiO_2 and (B) SnO_2/TiO_2 core/shell structures in acetonitrile/aqueous sodium acetate buffer (0.1 M, pH 4.6) mixed solvent electrolytes. Pump: 400 nm with a pulse energy of 200 μJ.

The OPTP traces for **RuP**-sensitized TiO_2 electrodes, shown in Figure 2A, exhibit a two-step injection process as previously reported, consistent with injection from the ^{1}MLCT and ^{3}MLCT excited states, respectively.[36,49] Therefore, the data were fit to a double exponential function with the first exponential corresponding to ultrafast injection from the ^{1}MLCT excited state and second being a stretched exponential corresponding to injection from the ^{3}MLCT excited state. The fitting function is shown below in eq 4, where ΔTHz is the total percent change in THz amplitude, ΔTHz_{PPC} is the total relative injection amplitude in terms of positive photoconductivity (PPC), t_{pump} is the time delay, A_1 is the relative injection amplitude from the ^{1}MLCT excited state, τ_1 is the injection lifetime from the ^{1}MLCT excited state fixed at 25 fs based on a previous literature report,[50] A_3 is the relative injection amplitude from the ^{3}MLCT excited state, τ_3 is the injection lifetime from the ^{3}MLCT excited state, β is the stretching parameter fixed at 0.8 to enable reliable comparison of ^{3}MLCT injection lifetimes, ⊗ represents a convolution, and G_{IRF} is a Gaussian instrument response function with a 0.6 ps full width at half-maximum.

$$\Delta THz(t_{pump}) = \Delta THz_{PCC}\left\{A_1\left[\exp\left(\frac{t_{pump}}{\tau_1}\right) - 1\right] + A_3\left[\exp\left(\left(\frac{t_{pump}}{\tau_3}\right)^{\beta}\right) - 1\right]\right\} \otimes G_{IRF} \tag{4}$$

The expectation value of the distribution of injection lifetimes from the ^{3}MLCT state characterized by the stretched exponential ($\langle\tau_3\rangle$) was calculated using eq 5 as shown below, where Γ is the gamma function and other variables are as previously described.[51,52]

$$\langle\tau_3\rangle = \frac{\tau_3}{\beta}\Gamma\left(\frac{1}{\beta}\right) \tag{5}$$

Notably, the relative injection yield at long times (i.e., ΔTHz_∞ defined as ΔTHz_{PPC}, Figure 3A **gray bars**) decreased with increasing acetonitrile concentration, consistent with thin film actinometry measurements obtained using nanosecond TAS. The relative contributions from A_1 and A_3 remained constant within the uncertainty of the fits for electrolytes containing acetate buffer, while the pure acetonitrile solvent exhibited enhanced ultrafast injection from the ^{1}MLCT excited state. In samples containing acetate buffer, the slower lifetime attributed to injection from the ^{3}MLCT excited state denoted as $\langle\tau_3\rangle$ increased monotonically with increasing acetonitrile concentration, while the pure acetonitrile sample exhibited an intermediate rate similar to the sample containing 50% acetonitrile (Figure 3B, **gray circles**). Because the total yields are different in each of the electrolyte solutions, normalized data are plotted in Figure S6 for easier comparison of the electron injection dynamics.

In contrast to measurements on TiO_2, electron injection into SnO_2/TiO_2 core/shell structures, as shown in Figure 2B, resulted in complicated photoconductivity dynamics with three distinct processes: two from PPC and one from negative photoconductivity (NPC). Because of the emergence of the NPC feature in core/shell structures, the assignments of electron transfer processes corresponding to specific **RuP** excited states are less clear than in TiO_2 (vide infra, Discussion). Therefore, the data in Figure 2B were fit to a function with an additional exponential term to describe the NPC process as shown in eq 6, where ΔTHz_{NPC} is the total amplitude of NPC, τ_{NPC} is the NPC lifetime, and other variables are as previously described.

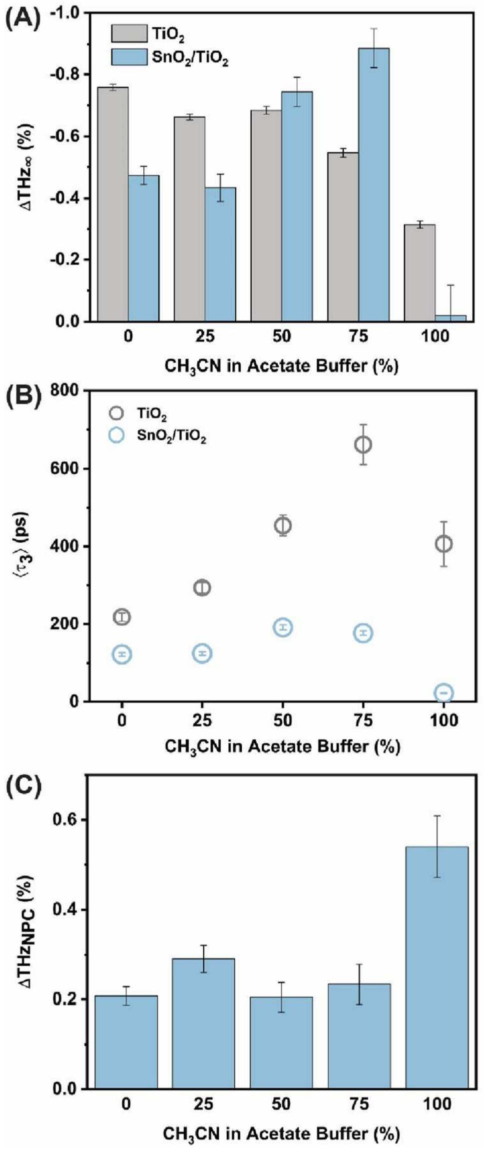

Figure 3. (A) Relative electron injection efficiency for **RuP**-sensitized TiO_2 (gray) and SnO_2/TiO_2 core/shell structure (blue) determined from optical-pump THz-probe (OPTP) measurements in terms of the total change in THz amplitude at long times denoted as ΔTHz_∞. (B) Expectation value of the lifetime from the slow ^{3}MLCT electron injection component. (C) Negative photoconductivity (ΔTHz_{NPC}) for **RuP**-sensitized SnO_2/TiO_2 core/shell structures.

$$\Delta THz(t_{pump}) = \left(\Delta THz_{PCC}\left\{A_1\left[\exp\left(\frac{t_{pump}}{\tau_1}\right) - 1\right] + A_3\left[\exp\left(\left(\frac{t_{pump}}{\tau_3}\right)^{\beta}\right) - 1\right]\right\} + \Delta THz_{NPC}\left[\exp\left(\frac{t_{pump}}{\tau_{NPC}}\right) - 1\right]\right) \otimes G_{IRF} \tag{6}$$

In the SnO_2/TiO_2 core/shell structures, the relative injection yield at long times (i.e., ΔTHz_∞ defined as $\Delta THz_{PPC} + \Delta THz_{NPC}$, Figure 3A **blue bars**) increased as a function of acetonitrile concentration for all mixed electrolytes containing acetate buffer. However, the pure acetonitrile solvent exhibited a low injection yield compared to the mixed electrolytes containing acetate buffer. This was consistent with thin-film actinometry measurements. Additionally, consistent with the results for TiO_2 samples, the relative contributions from A_1 and A_3 remained constant within the uncertainty of the fits for electrolytes containing acetate buffer but exhibited a large increase in A_1 for pure acetonitrile. The $\langle\tau_3\rangle$ injection lifetime in the SnO_2/TiO_2 core/shell samples exhibited a similar trend to TiO_2, with the exception that the pure acetonitrile sample had the shortest $\langle\tau_3\rangle$ injection lifetime, corresponding to the fastest injection rate. The NPC amplitude (ΔTHz_{NPC}) remained approximately constant for samples containing acetate buffer and was significantly enhanced for the pure acetonitrile sample (Figure 3C). The lifetimes of the NPC feature (τ_{NPC}) occur on an ultrafast time scale near the instrument response limit. While this makes quantification challenging, τ_{NPC} appears to decrease slightly with increasing acetonitrile concentration (Table S5) and is consistent with the NPC lifetime reported by Swierk et al. for **RuP**-sensitized SnO_2/TiO_2 core/shell structures in 0.1 M $HClO_4$.[21]

To understand the observed differences in electron transfer rates in various electrolyte solutions from a thermodynamic perspective, the flat band potentials of the semiconductor electrodes were measured by probing the absorption of the electrons in the conduction band. With dye molecules adsorbed on the electrode surface, the Fermi levels of the electrode and the molecule equilibrate, affecting the band bending near the semiconductor/molecule interface. Under cathodic bias, electrons compensate the positive charge of the space charge region and flatten the conduction and valence bands. At the flat band potential, the space charge region is fully compensated. The flat band potential is affected by the electrolyte and any adsorbed molecules or ions at the semiconductor/solution interface (Scheme 1).

Scheme 1. Dye-Adsorbed Photoelectrode in Depletion (Left) and Under Negative Bias at the Flat Band Potential (Right)

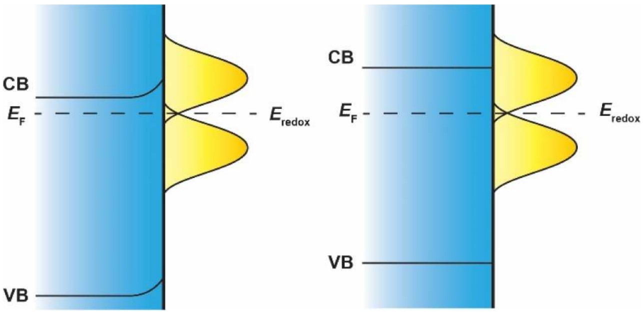

In Figure 4, when the electrode potential is scanned cathodically beyond the flat band potential, electrons accumulate in the conduction band and give rise to a strong absorption at 780 nm. Thus, the onset potential of the absorption can be used to measure the flat band potentials of the electrodes. The details of flat band potential measurements are shown in (Figures S7, S8 and Tables S6, S7).

As the acetonitrile content of the electrolyte is increased, the flat band potentials of the TiO_2 and core/shell electrodes shift

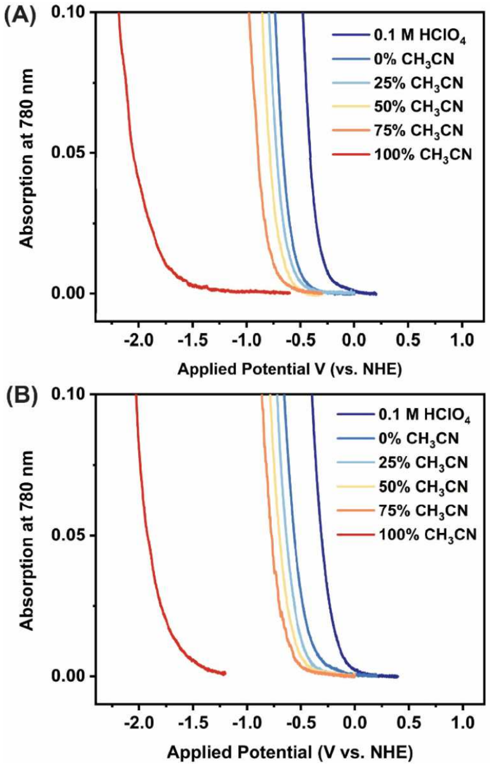

Figure 4. Absorbance of dye-sensitized (A) mesoporous TiO_2 and (B) SnO_2/TiO_2 electrodes in 0.1 M perchloric acid and 0.1 M tetra(*n*-butyl)ammonium perchlorate in acetonitrile/aqueous sodium acetate butter mixed solutions at 780 nm under applied potentials (electrodes in 100% CH_3CN were not sensitized in order to prevent the reduction of the sensitizer). Scan rate: −1 mV/5 s.

gradually to more negative potentials. In anhydrous acetonitrile containing 0.1 M tetra(*n*-butyl)ammonium perchlorate, the flat band potentials of both the TiO_2 and core/shell electrodes are shifted dramatically (by ca. −1 V) relative to the 75% CH_3CN electrolyte. Comparing the mesoporous TiO_2 and the core/shell electrodes at the same electrolyte compositions (Table 1), the flat band potentials of the core/shell electrodes are ∼100−200 mV more positive than those of the TiO_2 electrodes, consistent with the conduction band edge potential of SnO_2 being more positive than that of TiO_2.

Table 1. Flat Band Potentials of RuP$^{3+/2+}$ Functionalized Electrodes and Reduction Potentials of Adsorbed RuP$^{3+/2+}$ in Different Solvent Mixtures

electrolyte[a]	E_{FB} (TiO_2) (V)[b]	E_{FB} (SnO_2/TiO_2) (V)[b]	E (**RuP**$^{3+/2+}$)(V)[b]
0.1 M $HClO_4$	-0.13 ± 0.01	-0.01 ± 0.02	1.35
0% CH_3CN	-0.39 ± 0.01	-0.20 ± 0.07	1.36
25% CH_3CN	-0.44 ± 0.02	-0.32 ± 0.02	1.38
50% CH_3CN	-0.51 ± 0.04	-0.40 ± 0.01	1.38
75% CH_3CN	-0.58 ± 0.02	-0.51 ± 0.04	1.36
100% CH_3CN	-1.56 ± 0.10	-1.40 ± 0.05	1.56

[a] The electrolyte mixtures are denoted as the volume percentage of 0.1 M tetra(*n*-butyl)ammonium perchlorate in acetonitrile solution and 0.1 M sodium acetate buffer (pH 4.6). [b] Potentials vs NHE.

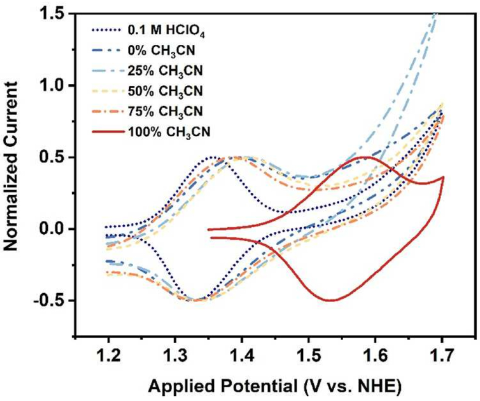

Figure 5. Cyclic voltammograms of ITO|**RuP** electrodes in 0.1 M tetra(*n*-butyl)ammonium perchlorate in acetonitrile/aqueous sodium acetate buffer (0.1 M, pH 4.6) mixtures. Scan rate 50 mV/s.

The reduction potential of **RuP**$^{3+/2+}$ adsorbed onto ITO electrodes was measured in different electrolyte solutions by cyclic voltammetry (Figure 5) and is listed in Table 1. ITO|**RuP**$^{2+}$ in acetonitrile has the most positive value of E(**RuP**$^{3+/2+}$) (1.56 V vs NHE), whereas the potential in acidic aqueous solutions shifted to 1.35 V vs NHE. In the aqueous/acetonitrile mixed electrolytes, the reduction potentials shifted to slightly more anodic values relative to 0.1 M $HClO_4$.

■ DISCUSSION

The driving force is an important measure for interfacial charge transfer in different solvent environments as it helps to understand the trends in electron injection efficiency. The charge transfer processes and the corresponding driving forces for electron transfer at the semiconductor/molecule interface are illustrated in Scheme 2.

The driving force for electron injection is proportional to the difference between the excited state reduction potential of the molecule and the flat band potential of the semiconductor:

$$\Delta G^{\circ}_{\text{inj}} = -F(E_{\text{FB}} - E^{\circ\prime}(\mathbf{RuP}^{3+/2+*})) \tag{7}$$

Electrons are injected into the semiconductor from both the excited singlet MLCT state (^{1}MLCT) and the triplet MLCT state (^{3}MLCT). For **RuP** adsorbed on anatase TiO_2, the excitation energy of the triplet MLCT, ΔG(^{3}MLCT), is 2.53 eV, and the singlet MLCT, ΔG(^{1}MLCT), is 2.70 eV. For **RuP** adsorbed on SnO_2/TiO_2 core/shell electrodes, ΔG(^{3}MLCT) is 2.46 eV and ΔG(^{1}MLCT) is 2.68 eV, according to a previous study.[36] Assuming that the excitation energy of the molecule is the same in different solvents, the excited state potentials can be calculated. The driving forces for electron injection are calculated according to eq 7. and the results are listed in Table 2.

In 0.1 M $HClO_4$ solutions, the driving force for electron injection is the largest due to the positive shift in the flat band potential that is induced by proton intercalation. In acetonitrile, the flat band potentials of the semiconductor electrodes are shifted to potentials more negative than the **RuP**$^{3+/2+}$ potential in the ^{3}MLCT excited state, thus resulting in slow injection from that state. This is also supported by the OPTP data (Tables S3 and S5). In acetonitrile, most of the injected electrons come from the more energetic ^{1}MLCT excited state and ^{3}MLCT injection is limited to lower-lying trap states that are not observable via OPTP due to their low carrier mobility.

The driving force for back electron transfer (charge recombination) can be calculated by the energy difference

Scheme 2. Free Energy Driving Forces for Excited State Electron Injection and Recombination at TiO_2 (Left) and SnO_2/TiO_2 Core/Shell Electrodes (Right)

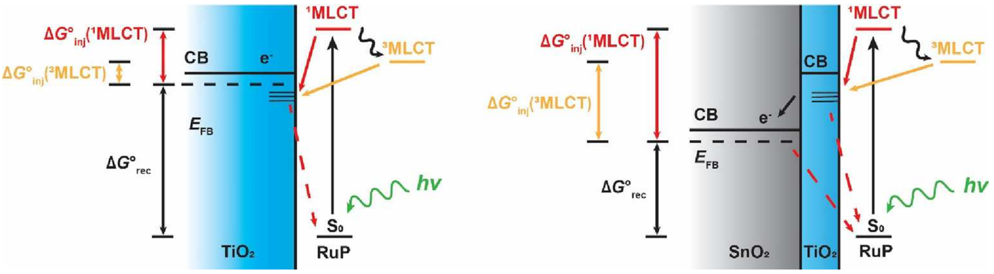

Table 2. Driving Forces for Interfacial Charge Transfer at $RuP^{3+/2+}$ Functionalized Electrodes in Electrolyte Mixtures

electrolyte[a]	ΔG°_{inj} ($^3MLCT \rightarrow TiO_2$)(eV)	ΔG°_{inj} ($^1MLCT \rightarrow TiO_2$)(eV)	ΔG°_{rec} (TiO_2) (eV)	ΔG°_{inj} ($^3MLCT \rightarrow SnO_2/TiO_2$)(eV)	ΔG°_{inj} ($^1MLCT \rightarrow SnO_2/TiO_2$)(eV)	ΔG°_{rec} (SnO_2/TiO_2) (eV)
0.1 M $HClO_4$	−1.05	−1.22	−1.48	−1.10	−1.32	−1.36
0% CH_3CN	−0.78	−0.95	−1.75	−0.90	−1.12	−1.56
25% CH_3CN	−0.71	−0.88	−1.82	−0.76	−0.98	−1.70
50% CH_3CN	−0.64	−0.81	−1.89	−0.68	−0.90	−1.78
75% CH_3CN	−0.59	−0.76	−1.94	−0.59	−0.81	−1.87
100% CH_3CN	-	-	−3.12	-	-	−2.96

[a] The electrolyte mixtures are denoted as the volume percentages of 0.1 M tetra(*n*-butyl)ammonium perchlorate in acetonitrile solution and 0.1 M aqueous sodium acetate buffer (pH 4.6).

between the flat band potentials of the semiconductor and the reduction potential of the molecules at ground state:

$$\Delta G^\circ_{rec} = -F(E^{\circ\prime}(\mathbf{RuP}^{3+/2+}) - E_{FB}) \tag{8}$$

The ground state reduction potential of surface-adsorbed $\mathbf{RuP}^{3+/2+}$ is relatively constant in aqueous and mixed electrolytes and is about 200 mV more anodic in the acetonitrile electrolyte. From Table 2, it is clear that the driving force for charge recombination increases with increasing acetonitrile concentration, consistent with the progressively negative shift in the semiconductor flat band potential.

When analyzing the effects of electrolyte composition, there are two factors that play a major role in modulating the electron injection efficiency and dynamics: (1) the energetics, which are dominated by the shift of the flat band potential relative to the reduction potentials of the sensitizer, and (2) the dielectric constant of the electrolyte. Earlier studies have shown that the lower dielectric constant in the electric double layer affects the reorganization energy for charge transfer.[44] Here we note that the static dielectric constant decreases monotonically from ~78 to ~35 as the acetonitrile concentration increases.[53,54]

In Figures 1 and 3, **RuP**-sensitized TiO_2 shows a trend of decreasing injection efficiency with increasing acetonitrile concentration, as measured by both nanosecond transient absorption and OPTP. At higher concentrations of acetonitrile, the cathodic shift in flat band potential lowers the driving force for excited state electron injection into TiO_2. A more complex trend is observed with **RuP**-sensitized SnO_2/TiO_2 core/shell electrodes. Mixed electrolytes gave higher injection efficiencies in both nanosecond transient absorption measurements and OPTP measurements, relative to purely aqueous or acetonitrile solutions. We can interpret this trend in terms of the two-step injection process illustrated in Scheme 2. With core/shell electrodes, the rate of electron injection into the SnO_2 core depends on the driving force for electron transfer between the shell and the core. The flat band potential of the TiO_2 shell is regulated by the composition of the electrolyte. Having no direct contact with the electrolyte, the flat band potential of the SnO_2 core remains relatively constant. Electrons injected into the trap states in the TiO_2 shell can either transfer to the SnO_2 core or recombine with the oxidized sensitizer. Consequently, the yield of electrons reaching the SnO_2 core increases with increasing concentrations of acetonitrile as the flat band potential of TiO_2 shifts more cathodically. For pure acetonitrile, the very cathodic flat band potential of the TiO_2 shell inhibits the injection of electrons from the dye, leading to lower injection efficiency.

Interestingly, **RuP**-sensitized SnO_2/TiO_2 core/shell electrodes exhibited complicated ultrafast behavior with both PPC and NPC components in the OPTP measurements (Figure 2B). The NPC effect is most pronounced in pure acetonitrile, but it is present in solvent mixtures as well. A small NPC effect had previously been observed by Swierk et al. for **RuP**-sensitized SnO_2/TiO_2 core/shell electrodes in 0.1 M $HClO_4$, and the effect was assigned to electron trapping in nonmobile states in the TiO_2 shell and/or at the SnO_2/TiO_2 interface.[21] However, Swierk et al. did not observe any net NPC (i.e., $\Delta THz > 0\%$), while we observed net NPC in three of the five electrolyte compositions. The assignment of trapping in the TiO_2 shell and/or at the SnO_2/TiO_2 interface from only photoinjected carriers is inconsistent with net NPC, so we offer an alternative explanation to better describe this behavior. We hypothesize that the NPC component is due to trapping at the SnO_2/TiO_2 interface that occurs from both photoinjected electrons and intrinsic carriers in the conduction band of SnO_2

(i.e., "dark" free electrons). Previous work on SnO_2/TiO_2 core/shell structures has suggested the formation of a $Sn_xTi_{1-x}O_2$ solid solution at the core/shell interface that is more easily reduced than either SnO_2 or TiO_2, suggesting that carrier localization in this interfacial region is thermodynamically favorable.[55] In addition, there are likely a high density of defect states at the SnO_2/TiO_2 interface that could act as these lower energy, low mobility trap states.[21,56] Electron injection results in an increase in the positive charge of oxidized dye molecules. The positive surface charge induces an electric field across the TiO_2 shell which causes carrier trapping of both photoinjected and intrinsic electrons at the SnO_2/TiO_2 interface, thereby lowering the conductivity relative to the dark state (i.e., $t_{\mathrm{pump}} < 0$ ps). The differences in total amplitude of the NPC component (ΔTHz_{NPC}) can be rationalized in terms of charge screening by the electrolyte at the interface. The lower dielectric constant of pure acetonitrile results in less efficient screening of the surface charge, causing significant trapping at the SnO_2/TiO_2 interface and resulting in a large NPC relative to the dark state. Electrolytes containing aqueous acetate buffer exhibit nearly identical relative NPC relative to the dark state, even though they have different bulk dielectric constants. This suggests that the presence of ions in the EDL is the dominant factor in determining the interfacial dielectric constant, providing more effective screening of the surface charge for electrolyte compositions containing aqueous acetate buffer. The formation of the injection-induced electric field is shown in Scheme 3.

CONCLUSIONS

Photoinduced electron injection efficiencies of the surface-adsorbed dye molecules on TiO_2 and SnO_2/TiO_2 core/shell electrodes were measured by nanosecond transient absorption and ultrafast optical-pump terahertz-probe spectroscopy as a function of electrolyte composition. For TiO_2, the injection efficiency decreases with the acetonitrile fraction in acetate buffer electrolytes. In contrast, the injection efficiencies increase with the concentration of acetonitrile at SnO_2/TiO_2 core/shell electrodes. For both structures in pure acetonitrile, the injection efficiencies decreased significantly. The flat band potential of TiO_2 shifts negatively with increasing concentrations of acetonitrile. The negative shift in the flat band potential lowers the driving force for electron injection from the dye molecules to trap states in the TiO_2 shell but increases the driving force for electron transfer from the TiO_2 shell to the SnO_2 core. During the photoinduced electron injection in SnO_2/TiO_2 core/shell structures, a net negative photoconductivity was observed for the first time in a dye-sensitized metal oxide. The negative photoconductivity was attributed to the trapping of both photoinduced carriers and intrinsic carriers in the SnO_2 at the SnO_2/TiO_2 interface, lowering the overall conductivity relative to the dark state. This effect is most pronounced in the low-dielectric solvent which does not efficiently screen the positive charge at the TiO_2 surface after electron injection. This effect illustrates the importance of using electrolytes with high ionic strength and a high dielectric constant to facilitate charge injection into the core semiconductor. Modulating the solvent composition is thus a useful strategy for maximizing photoinduced electron injection yields in the core/shell electrodes that are used in the most efficient WS-DSPECs. In addition to changing the solvent environment as explored in this work, further study and optimization of the core/shell interface may provide an additional parameter for tuning charge carrier dynamics in these systems. Understanding the details of charge transfer processes at the semiconductor/molecule interface could thus inform the design of more efficient energy conversion devices that are based on dye sensitization of core/shell semiconductors.

Scheme 3. Formation of an Injection-Induced Electric Field Across the TiO_2 Shell

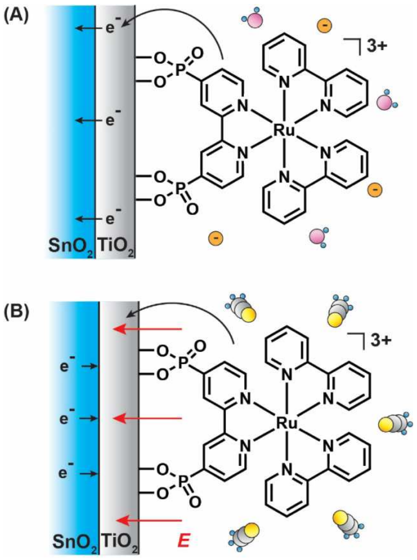

(A) In aqueous buffer solutions, the positive surface charge is effectively screened by electrolyte ions. (B) In acetonitrile, the surface charge is not efficiently screened due to the lower dielectric constant and the lack of ions, resulting in the trapping of photoinduced and intrinsic carriers at the SnO_2/TiO_2 interface

ASSOCIATED CONTENT

Supporting Information

The Supporting Information is available free of charge at https://pubs.acs.org/doi/10.1021/jacs.4c05187.

TEM images and EDS mapping of the SnO_2/TiO_2 core/shell structure; absorption spectra of sensitized TiO2 and SnO2/TiO2 electrodes; kinetics of the relaxation of **RuP** in excited states; fit parameters of nanosecond transient absorption measurements; CV of ferrocene in acetonitrile; normalized OPTP traces; fit parameters from OPTP measurements; determination of flat band potentials; temperature-dependent kinetics of electron recombination of both TiO_2 and SnO_2/TiO_2 in different solvent mixtures (PDF)

AUTHOR INFORMATION

Corresponding Author

Thomas E. Mallouk − *Department of Chemistry, University of Pennsylvania, Philadelphia, Pennsylvania 19104, United States;* orcid.org/0000-0003-4599-4208;
Email: mallouk@sas.upenn.edu

Authors

Langqiu Xiao − *Department of Chemistry, University of Pennsylvania, Philadelphia, Pennsylvania 19104, United States;* orcid.org/0000-0003-0695-3075

Jacob A. Spies − *Department of Chemistry, University of California, Berkeley, California 94720, United States; Department of Chemistry, Yale University, New Haven, Connecticut 06520, United States;* orcid.org/0000-0002-0148-4823

Colton J. Sheehan − *Department of Chemistry, University of Pennsylvania, Philadelphia, Pennsylvania 19104, United States;* orcid.org/0000-0002-0284-5627

Zichen Zeng − *Department of Chemistry, University of Pennsylvania, Philadelphia, Pennsylvania 19104, United States*

Yunhan Gao − *Department of Chemistry, University of Pennsylvania, Philadelphia, Pennsylvania 19104, United States*

Tianyue Gao − *Department of Chemistry, University of Pennsylvania, Philadelphia, Pennsylvania 19104, United States*

Annika Ehrlacher − *Department of Chemistry, University of Pennsylvania, Philadelphia, Pennsylvania 19104, United States*

Michael W. Zuerch − *Department of Chemistry, University of California, Berkeley, California 94720, United States;* orcid.org/0000-0001-5151-2119

Gary W. Brudvig − *Department of Chemistry, Yale University, New Haven, Connecticut 06520, United States;* orcid.org/0000-0002-7040-1892

Complete contact information is available at:
https://pubs.acs.org/10.1021/jacs.4c05187

Notes

The authors declare no competing financial interest.

■ ACKNOWLEDGMENTS

The authors thank Shengsong Yang for the help with TEM and Xiayan Ji for the help with data analysis. This work was supported by the Office of Basic Energy Sciences, Division of Chemical Sciences, Geosciences, and Energy Biosciences, Department of Energy, under contract DE-SC0019781. This work was carried out in part at the Singh Center for Nanotechnology, which is supported by the NSF National Nanotechnology Coordinated Infrastructure Program under grant NNCI-2025608. J.A.S. acknowledges support from the Arnold O. Beckman Postdoctoral Fellowship Program. C.J.S. acknowledges support from the National Science Foundation Graduate Research Fellowship under Grant No. DGE-1845298. G.W.B. acknowledges support from the U.S. Department of Energy, Chemical Sciences, Geosciences, and Biosciences Division, Office of Basic Energy Science under contract DE-FG02-07ER15909. M.W.Z acknowledges support from the National Science Foundation (NSF-DMR 2247363).

■ REFERENCES

(1) Niu, F.; Wang, D.; Li, F.; Liu, Y.; Shen, S.; Meyer, T. J. Hybrid Photoelectrochemical Water Splitting Systems: From Interface Design to System Assembly. *Adv. Energy Mater.* **2020**, *10*, 1900399.

(2) Yun, S.; Vlachopoulos, N.; Qurashi, A.; Ahmad, S.; Hagfeldt, A. Dye Sensitized Photoelectrolysis Cells. *Chem. Soc. Rev.* **2019**, *48*, 3705−3722.

(3) Zhang, S.; Ye, H.; Hua, J.; Tian, H. Recent Advances in Dye-Sensitized Photoelectrochemical Cells for Water Splitting. *Energy Chem.* **2019**, *1*, 100015.

(4) Desilvestro, J.; Grätzel, M.; Kavan, L.; Moser, J.; Augustynski, J. Highly Efficient Sensitization of Titanium Dioxide. *J. Am. Chem. Soc.* **1985**, *107*, 2988−2990.

(5) Ren, Y.; Zhang, D.; Suo, J.; Cao, Y.; Eickemeyer, F. T.; Vlachopoulos, N.; Zakeeruddin, S. M.; Hagfeldt, A.; Grätzel, M. Hydroxamic Acid Pre-Adsorption Raises the Efficiency of Cosensitized Solar Cells. *Nature* **2023**, *613*, 60−65.

(6) Swierk, J. R.; McCool, N. S.; Mallouk, T. E. Dynamics of Electron Recombination and Transport in Water-Splitting Dye-Sensitized Photoanodes. *J. Phys. Chem. C* **2015**, *119*, 13858−13867.

(7) Brennan, B. J.; Regan, K. P.; Durrell, A. C.; Schmuttenmaer, C. A.; Brudvig, G. W. Solvent Dependence of Lateral Charge Transfer in a Porphyrin Monolayer. *ACS Energy Lett.* **2017**, *2*, 168−173.

(8) Youngblood, W. J.; Lee, S.-H. A.; Maeda, K.; Mallouk, T. E. Visible Light Water Splitting Using Dye-Sensitized Oxide Semiconductors. *Acc. Chem. Res.* **2009**, *42*, 1966−1973.

(9) Zhao, Y.; Swierk, J. R.; Megiatto, J. D.; Sherman, B.; Youngblood, W. J.; Qin, D.; Lentz, D. M.; Moore, A. L.; Moore, T. A.; Gust, D.; Mallouk, T. E. Improving the Efficiency of Water Splitting in Dye-Sensitized Solar Cells by Using a Biomimetic Electron Transfer Mediator. *Proc. Natl. Acad. Sci. U. S. A.* **2012**, *109*, 15612−15616.

(10) Song, W.; Chen, Z.; Glasson, C. R. K.; Hanson, K.; Luo, H.; Norris, M. R.; Ashford, D. L.; Concepcion, J. J.; Brennaman, M. K.; Meyer, T. J. Interfacial Dynamics and Solar Fuel Formation in Dye-Sensitized Photoelectrosynthesis Cells. *Chem. Phys. Chem.* **2012**, *13*, 2882−2890.

(11) Huang, Z.; Geletii, Y. V.; Musaev, D. G.; Hill, C. L.; Lian, T. Spectroscopic Studies of Light-Driven Water Oxidation Catalyzed by Polyoxometalates. *Ind. Eng. Chem. Res.* **2012**, *51*, 11850−11859.

(12) Brimblecombe, R.; Koo, A.; Dismukes, G. C.; Swiegers, G. F.; Spiccia, L. Solar Driven Water Oxidation by a Bioinspired Manganese Molecular Catalyst. *J. Am. Chem. Soc.* **2010**, *132*, 2892−2894.

(13) Chen, H. Y.; Ardo, S. Direct Observation of Sequential Oxidations of a Titania-Bound Molecular Proxy Catalyst Generated through Illumination of Molecular Sensitizers. *Nat. Chem.* **2018**, *10*, 17−23.

(14) Jiang, J.; Spies, J. A.; Swierk, J. R.; Matula, A. J.; Regan, K. P.; Romano, N.; Brennan, B. J.; Crabtree, R. H.; Batista, V. S.; Schmuttenmaer, C. A.; Brudvig, G. W. Direct Interfacial Electron Transfer from High-Potential Porphyrins into Semiconductor Surfaces: A Comparison of Linkers and Anchoring Groups. *J. Phys. Chem. C* **2018**, *122*, 13529−13539.

(15) Xu, P.; Gray, C. L.; Xiao, L.; Mallouk, T. E. Charge Recombination with Fractional Reaction Orders in Water-Splitting Dye-Sensitized Photoelectrochemical Cells. *J. Am. Chem. Soc.* **2018**, *140*, 11647−11654.

(16) Alibabaei, L.; Sherman, B. D.; Norris, M. R.; Brennaman, M. K.; Meyer, T. J. Visible Photoelectrochemical Water Splitting into H_2 and O_2 in a Dye-Sensitized Photoelectrosynthesis Cell. *Proc. Natl. Acad. Sci. U. S. A.* **2015**, *112*, 5899−5902.

(17) Xiao, L.; Yu, Y.; Schultz, E. L.; Stach, E. A.; Mallouk, T. E. Electron Transport in Dye-Sensitized TiO_2 Nanowire Arrays in Contact with Aqueous Electrolytes. *J. Phys. Chem. C* **2020**, *124*, 22003−22010.

(18) Gao, Y.; Ding, X.; Liu, J.; Wang, L.; Lu, Z.; Li, L.; Sun, L. Visible Light Driven Water Splitting in a Molecular Device with Unprecedentedly High Photocurrent Density. *J. Am. Chem. Soc.* **2013**, *135*, 4219−4222.

(19) Wang, D.; Wang, L.; Brady, M. D.; Dares, C. J.; Meyer, G. J.; Meyer, T. J.; Concepcion, J. J. Self-Assembled Chromophore-Catalyst Bilayer for Water Oxidation in a Dye-Sensitized Photoelectrosynthesis Cell. *J. Phys. Chem. C* **2019**, *123*, 30039−30045.

(20) Xu, P.; Mallouk, T. E. Charge Transfer Dynamics in Aqueous Dye-Sensitized Photoelectrochemical Cells: Implications for Water Splitting Efficiency. *J. Phys. Chem. C* **2019**, *123*, 299−305.

(21) Swierk, J. R.; McCool, N. S.; Nemes, C. T.; Mallouk, T. E.; Schmuttenmaer, C. A. Ultrafast Electron Injection Dynamics of

Photoanodes for Water-Splitting Dye-Sensitized Photoelectrochemical Cells. *J. Phys. Chem. C* **2016**, *120*, 5940−5948.

(22) Koops, S. E.; O'Regan, B. C.; Barnes, P. R. F.; Durrant, J. R. Parameters Influencing the Efficiency of Electron Injection in Dye-Sensitized Solar Cells. *J. Am. Chem. Soc.* **2009**, *131*, 4808−4818.

(23) Munoz-Garcia, A. B.; Benesperi, I.; Boschloo, G.; Concepcion, J. J.; Delcamp, J. H.; Gibson, E. A.; Meyer, G. J.; Pavone, M.; Pettersson, H.; Hagfeldt, A.; Freitag, M. Dye-Sensitized Solar Cells Strike Back. *Chem. Soc. Rev.* **2021**, *50*, 12450−12550.

(24) O'Regan, B.; Grätzel, M. A Low-Cost, High-Efficiency Solar Cell Based on Dye-Sensitized Colloidal TiO_2 Films. *Nature* **1991**, *354*, 737−740.

(25) Bella, F.; Gerbaldi, C.; Barolo, C.; Grätzel, M. Aqueous Dye-Sensitized Solar Cells. *Chem. Soc. Rev.* **2015**, *44*, 3431−3473.

(26) Law, C.; Pathirana, S. C.; Li, X.; Anderson, A. Y.; Barnes, P. R. F.; Listorti, A.; Ghaddar, T. H.; O′regan, B. C. Water-Based Electrolytes for Dye-Sensitized Solar Cells. *Adv. Mater.* **2010**, *22*, 4505−4509.

(27) Bergeron, B. V.; Kelly, C. A.; Meyer, G. J. Thin Film Actinometers for Transient Absorption Spectroscopy: Applications to Dye-Sensitized Solar Cells. *Langmuir* **2003**, *19*, 8389−8394.

(28) Turner, G. M.; Beard, M. C.; Schmuttenmaer, C. A. Carrier Localization and Cooling in Dye-Sensitized Nanocrystalline Titanium Dioxide. *J. Phys. Chem. B* **2002**, *106*, 11716−11719.

(29) Lyon, L. A.; Hupp, J. T. Energetics of Semiconductor Electrode/Solution Interfaces: EQCM Evidence for Charge-Compensating Cation Adsorption and Intercalation during Accumulation Layer Formation in the Titanium Dioxide/Acetonitrile System. *J. Phys. Chem.* **1995**, *99*, 15718−15720.

(30) McCool, N. S.; Swierk, J. R.; Nemes, C. T.; Schmuttenmaer, C. A.; Mallouk, T. E. Dynamics of Electron Injection in SnO_2/TiO_2 Core/Shell Electrodes for Water-Splitting Dye-Sensitized Photoelectrochemical Cells. *J. Phys. Chem. Lett.* **2016**, *7*, 2930−2934.

(31) Montalti, M.; Wadhwa, S.; Kim, W. Y.; Kipp, R. A.; Schmehl, R. H. Luminescent Ruthenium(II) Bipyridyl-Phosphonic Acid Complexes: pH Dependent Photophysical Behavior and Quenching with Divalent Metal Ions. *Inorg. Chem.* **2000**, *39*, 76−84.

(32) Trammell, S. A.; Moss, J. A.; Yang, J. C.; Nakhle, B. M.; Slate, C. A.; Odobel, F.; Sykora, M.; Erickson, B. W.; Meyer, T. J. Sensitization of TiO_2 by Phosphonate-Derivatized Proline Assemblies. *Inorg. Chem.* **1999**, *38*, 3665−3669.

(33) McCool, N. S.; Swierk, J. R.; Nemes, C. T.; Saunders, T. P.; Schmuttenmaer, C. A.; Mallouk, T. E. Proton-Induced Trap States, Injection and Recombination Dynamics in Water-Splitting Dye-Sensitized Photoelectrochemical Cells. *ACS Appl. Mater. Interfaces* **2016**, *8*, 16727−16735.

(34) Ito, S.; Chen, P.; Comte, P.; Nazeeruddin, M. K.; Liska, P.; Péchy, P.; Grätzel, M. Fabrication of Screen-Printing Pastes from TiO_2 Powders for Dye-Sensitised Solar Cells. *Prog. Photovoltaics: Res. Appl.* **2007**, *15*, 603−612.

(35) Ravishankar, S.; Riquelme, A.; Sarkar, S. K.; Garcia-Batlle, M.; Garcia-Belmonte, G.; Bisquert, J. Intensity-Modulated Photocurrent Spectroscopy and Its Application to Perovskite Solar Cells. *J. Phys. Chem. C* **2019**, *123*, 24995−25014.

(36) Spies, J. A.; Swierk, J. R.; Kelly, H. R.; Capobianco, M. D.; Regan, K. P.; Batista, V. S.; Brudvig, G. W.; Schmuttenmaer, C. A. Tuning the Conduction Band for Interfacial Electron Transfer: Dye-Sensitized $Sn_xTi_{1-X}O_2$ Photoanodes for Water Splitting. *ACS Appl. Energy Mater.* **2021**, *4*, 4695−4703.

(37) Spies, J. A.; Neu, J.; Tayvah, U. T.; Capobianco, M. D.; Pattengale, B.; Ostresh, S.; Schmuttenmaer, C. A. Terahertz Spectroscopy of Emerging Materials. *J. Phys. Chem. C* **2020**, *124*, 22335−22346.

(38) Spies, J. A.; Hilibrand, M. J.; Neu, J.; Ostresh, S.; Swierk, J. R.; Schmuttenmaer, C. A. Suspensions of Semiconducting Nanoparticles in Nafion for Transient Spectroscopy and Terahertz Photoconductivity Measurements. *Anal. Chem.* **2020**, *92*, 4187−4192.

(39) Kress, M.; Löffler, T.; Eden, S.; Thomson, M.; Roskos, H. G. Terahertz-Pulse Generation by Photoionization of Air with Laser Pulses Composed of Both Fundamental and Second-Harmonic Waves. *Opt. Lett.* **2004**, *29*, 1120−1122.

(40) Bartel, T.; Reimann, K.; Woerner, M.; Elsaesser, T. Generation of THz Transients with High Electric-Field Amplitudes. *Opt. InfoBase Conf. Pap.* **2005**, *30*, 2805−2807.

(41) Wu, Q.; Zhang, X.-C. Free-Space Electro-Optic Sampling of Terahertz Beams. *Appl. Phys. Lett.* **1995**, *67*, 3523−3525.

(42) Redmond, G.; Fitzmaurice, D. Spectroscopic Determination of Flatband Potentials for Polycrystalline TiO_2 Electrodes in Nonaqueous Solvents. *J. Phys. Chem.* **1993**, *97*, 1426−1430.

(43) Enright, B.; Redmond, G.; Fitzmaurice, D. Spectroscopic Determination of Flatband Potentials for Polycrystalline TiO_2 Electrodes in Mixed Solvent Systems. *J. Phys. Chem.* **1994**, *98*, 6195−6200.

(44) Bangle, R. E.; Schneider, J.; Piechota, E. J.; Troian-Gautier, L.; Meyer, G. J. Electron Transfer Reorganization Energies in the Electrode-Electrolyte Double Layer. *J. Am. Chem. Soc.* **2020**, *142*, 674−679.

(45) Hanson, K.; Brennaman, M. K.; Ito, A.; Luo, H.; Song, W.; Parker, K. A.; Ghosh, R.; Norris, M. R.; Glasson, C. R. K.; Concepcion, J. J.; Lopez, R.; Meyer, T. J. Structure-Property Relationships in Phosphonate-Derivatized, Ru^{II} Polypyridyl Dyes on Metal Oxide Surfaces in an Aqueous Environment. *J. Phys. Chem. C* **2012**, *116*, 14837−14847.

(46) Luo, H.; Song, W.; Hoertz, P. G.; Hanson, K.; Ghosh, R.; Rangan, S.; Brennaman, M. K.; Concepcion, J. J.; Binstead, R. A.; Bartynski, R. A.; Lopez, R.; Meyer, T. J. A Sensitized Nb_2O_5 Photoanode for Hydrogen Production in a Dye-Sensitized Photoelectrosynthesis Cell. *Chem. Mater.* **2013**, *25*, 122−131.

(47) Song, W.; Glasson, C. R. K.; Luo, H.; Hanson, K.; Brennaman, M. K.; Concepcion, J. J.; Meyer, T. J. Photoinduced Stepwise Oxidative Activation of a Chromophore−Catalyst Assembly on TiO_2. *J. Phys. Chem. Lett.* **2011**, *2*, 1808−1813.

(48) Knauf, R. R.; Kalanyan, B.; Parsons, G. N.; Dempsey, J. L. Charge Recombination Dynamics in Sensitized SnO_2/TiO_2 Core/Shell Photoanodes. *J. Phys. Chem. C* **2015**, *119*, 28353−28360.

(49) Pijpers, J. J. H.; Ulbricht, R.; Derossi, S.; Reek, J. N. H.; Bonn, M. Picosecond Electron Injection Dynamics in Dye-Sensitized Oxides in the Presence of Electrolyte. *J. Phys. Chem. C* **2011**, *115*, 2578−2584.

(50) Giokas, P. G.; Miller, S. A.; Hanson, K.; Norris, M. R.; Glasson, C. R. K.; Concepcion, J. J.; Bettis, S. E.; Meyer, T. J.; Moran, A. M. Spectroscopy and Dynamics of Phosphonate-Derivatized Ruthenium Complexes on TiO_2. *J. Phys. Chem. C* **2013**, *117*, 812−824.

(51) Regan, K. P.; Swierk, J. R.; Neu, J.; Schmuttenmaer, C. A. Frequency-Dependent Terahertz Transient Photoconductivity of Mesoporous SnO_2 Films. *J. Phys. Chem. C* **2017**, *121*, 15949−15956.

(52) Laher Ere, J.; Sornette, D. Stretched Exponential Distributions in Nature and Economy: ″Fat Tails″ with Characteristic Scales. *Eur. Phys. J. B* **1998**, *2*, 525−539.

(53) Gagliardi, L. G.; Castells, C. B.; Ràfols, C.; Rosés, M.; Bosch, E. Static Dielectric Constants of Acetonitrile/Water Mixtures at Different Temperatures and Debye-Hückel A and a_0B Parameters for Activity Coefficients. *J. Chem. Eng. Data* **2007**, *52*, 1103−1107.

(54) Venables, D. S.; Schmuttenmaer, C. A. Far-Infrared Spectra and Associated Dynamics in Acetonitrile-Water Mixtures Measured with Femtosecond THz Pulse Spectroscopy. *J. Chem. Phys.* **1998**, *108*, 4935−4944.

(55) James, E. M.; Bennett, M. T.; Bangle, R. E.; Meyer, G. J. Electron Localization and Transport in SnO_2/TiO_2 Mesoporous Thin Films: Evidence for a $SnO_2/Sn_xTi_{1-X}O_2/TiO_2$ Structure. *Langmuir* **2019**, *35*, 12694−12703.

(56) James, E. M.; Barr, T. J.; Meyer, G. J. Evidence for an Electronic State at the Interface between the SnO_2 Core and the TiO_2 Shell in Mesoporous SnO_2/TiO_2 Thin Films. *ACS Appl. Energy Mater.* **2018**, *1*, 859−867.